Chapter 2
Atomically Precise Nanoclusters as Electrocatalysts

Site Li and Rongchao Jin

Abstract This chapter summaries recent advances in electrocatalytic application of atomically precise metal nanoclusters (NCs). Metal nanoclusters with determined structures can serve as new model catalysts for electrochemical catalytic study at the atomic level and offer insights into the underlying mechanisms. In recent years, electrocatalysis by metal nanoclusters has been reported and shows promise in several important reactions, including oxygen reduction reaction, water splitting, and CO_2 reduction reaction. By tuning the structure/ligand of the metal nanoclusters, it is possible to achieve catalytic property modification at the atomic level. Overall, the new material of atomically precise metal nanoclusters holds great promise in precise control of catalytic properties and investigation of the fundamental catalytic mechanism at the atomic level.

Keywords Metal nanocluster · Atomic precision · X-ray structure · Electrocatalysis · Doping

2.1 Introduction

2.1.1 Atomically Precise Metal NCs

Atomically precise metal nanoclusters have attracted broad interest due to the crystal structure availability and unique properties in optical and catalysis applications [1–3]. Compared with the traditional plasmonic metal nanoparticles, the ultra-small NCs (<3 nm) show quantized electronic structures because of the quantum confinement effect [4]. As a result, a single atom change can significantly alter the properties of NCs. The UV-vis spectrum can be used as the "fingerprints" of NCs [5] because it shows certain distinct peaks for each size of NCs, rather than similar plasmonic peaks for regular nanoparticles. Similarly, the catalytic properties of various metal NCs can be totally different because of the major change in surface and electronic structure of

S. Li · R. Jin (✉)
Department of Chemistry, Carnegie Mellon University, Pittsburgh, PA 15213, USA
e-mail: rongchao@andrew.cmu.edu

P. W. N. M. van Leeuwen and C. Claver (eds.), *Recent Advances in Nanoparticle Catalysis*, Molecular Catalysis 1, https://doi.org/10.1007/978-3-030-45823-2_2

NCs with subtle difference in atom numbers or size. Therefore, it is of great interest to correlate the structure and catalytic application using NCs as model catalysts [6]. Indeed, it is possible to build up a library of NCs structure–catalytic properties since the number of reported NCs is large enough. This library might offer great insights into the interpretation of catalytic process and reaction mechanism, and further offer some guidelines in the future design and synthesis of new NCs.

2.1.2 Electrochemical Catalysis with Atomically Precise Metal NCs

The global energy crisis and pollution issues have driven scientists to investigate the alternatives of fossil fuels. One of the strategies is using the secondary energy (such as solar energy and wind energy) derived electricity to split water for producing H_2 as a clean energy source [7]. In the water splitting system, hydrogen is produced at the cathode through hydrogen evolution reaction (HER), and oxygen is formed at the anode through oxygen evolution reaction (OER). Currently, Pt group metals are proved to be the most effective catalysts in HER, while Ir/Ru materials are successful in OER. However, the high cost of noble metals has motivated scientists to study alternative catalysts for these reactions.

On the other hand, the obtained hydrogen from HER and other fuels, such as methanol, can be utilized in the fuel cell system. The fuel cell is an electrochemical device to efficiently transform chemical energy of fuel without combustion [8]. Due to its high efficiency and environmentally friendly properties, fuel cells have been used in vehicles [9]. Currently, the disadvantage of fuel cell technique is the oxygen reduction reaction (ORR) in cathode electrode. It is believed that the ORR is the rate limiting reaction with very sluggish kinetics because of multi-electron transfer during the reaction [10]. Similar to the HER, ORR also favors Pt as the catalyst. Therefore, alternative catalysts are yet to be found to reduce the high cost of noble metals.

Another popular electrochemical catalytic reaction is the CO_2 electrochemical reduction reaction (CO_2RR). In the past decades, the global warming has been considered as a serious issue caused by massive CO_2 emission. To relieve the climate change pressure, one of the solutions is to utilize CO_2 as a resource to produce industrial chemicals and fuels [11, 12]. In the CO_2RR, catalytic materials are required to overcome the intrinsic inertness of CO_2 molecules [13]. Among the catalyst candidates, Au and Ag have been extensively studied because of their high selectivity toward CO [14]. Besides, Cu is also a good catalyst because of its versatility to form various carbon hydrates and low price.

To design better catalytic materials, it is essential to understand the mechanism behind these catalytic reactions. Thus, it is of great importance to find a system to correlate the structure and catalytic properties. Previously, several strategies, including size control and morphology control, have been used to investigate the

relationships between structure and properties [15, 16]. For example, Zhu et al. [17] and Seoin et al. [18] reported the active site probing with Au catalysts of different morphologies from the view of experimental and computational modeling, respectively. Despite the well-designed experiment, the non-atomically monodispersed size of traditional nanomaterials significantly weakens the connection between the structure and properties.

In the past decades, the synthesis strategy of atomically precise metal NCs has been extensively investigated and a number of sizes of NCs between tens and hundreds of atoms (equivalent diameters ranging from sub-nanometer to ~2.2 nm) have been reported [1]. For applications as electrochemical catalytic materials, such NCs have several distinctive features such as high surface area and unique surface structure [19]. Besides, the atomic precision and crystal structure availability make metal NCs a perfect system to bridge the structure and properties.

In this chapter, several works about metal NCs as electrochemical catalysts are introduced with a focus on the atomic size effect, morphology effect, doping effect, and charge effect. The computational techniques used in the catalytic mechanism study are also summarized.

2.2 Synthesis and Structure Determination of Atomically Precise Metal NCs

2.2.1 Synthesis of Metal NCs

Here, we illustrate the size-focusing synthesis and structure determination using atomically precise $Au_{25}(SR)_{18}$ NCs as an example. Larger NCs such as $Au_{133}(SR)_{52}$ and $Au_{279}(SR)_{84}$ can also be synthesized by the size-focusing method [20, 21]. In the size-focusing method, a mixture of NCs with a controlled size distribution is first prepared by carefully controlling the ratio of gold precursor and reduction agent as well as other synthetic conditions. Then, the NCs mixture is subjected to size-focusing under harsh conditions, under which the unstable NCs decompose or convert to more stable ones. Eventually, only the most stable NCs can survive the size-focusing process [22].

In the case of Au_{25} [23, 24], the Au(III) salt is initially reduced to Au(I) by thiols at 0 °C in the first step. The as-obtained Au(I)-SR complex is then reduced by adding a $NaBH_4$ aqueous solution. Polydisperse NCs protected by thiolate are obtained after the reduction process. During the following size-focusing process, it can be observed from the evolution of the optical absorption spectra that the monodispersed Au_{25} NCs gradually become dominant, as shown in Fig. 2.1a. The mass spectrum also illustrates the molecular purity of Au_{25} (Fig. 2.1b).

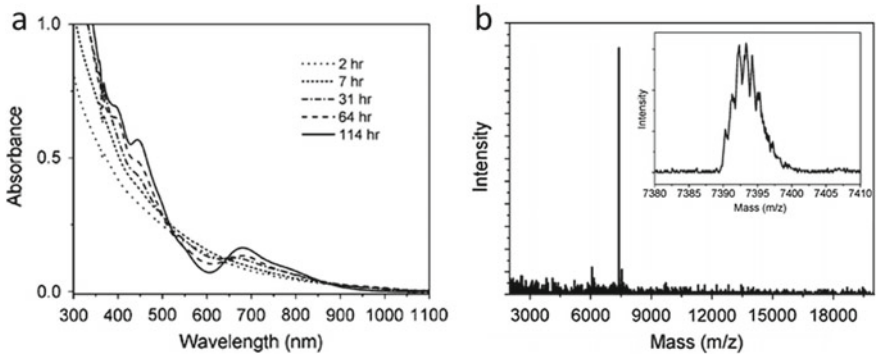

Fig. 2.1 **a** Evolution of the UV-vis spectra of the reaction product in the Au_{25} synthesis, **b** mass spectrometry analysis of Au_{25}. Adapted from Ref. [24]. Copyright 2009 Royal Society of Chemistry

2.2.2 Structure Determination of Metal NCs

The crystal structures of NCs can be determined by X-ray crystallography. In the case of Au_{25}, the structure comprises a Au_{13} icosahedral core and a $Au_{12}(SR)_{18}$ shell [23]. The Au_{12} shell can be dissected into six dimeric –S–Au–S–Au–S– staple motifs (Fig. 2.2). Due to the atomic precision and the determined crystal structure of metal NCs, it is of great interest to use NCs as catalysts for catalytic mechanism study. Especially for electrochemical catalysis, it is challenging to capture the intermediates during the catalytic process and thus very little is known about the mechanism. However, the well-defined structure of nanocluster catalysts can now facilitate the computational modeling, thus providing opportunities to reveal the mechanism behind electrochemical catalysis.

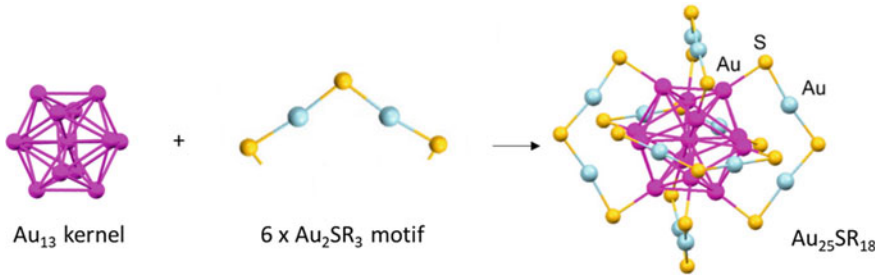

Fig. 2.2 Dissection of the Au_{25} cluster into Au_{13} kernel and six surface motifs. Adapted from Ref. [5]. Copyright 2012 American Chemical Society

2.3 Hydrogen Evolution Reaction with Metal NC Catalysts

The hydrogen evolution reaction (HER) occurs at the cathode when an external voltage is applied. The reaction can be described in three steps:

Volmer reaction:

$$H^+ + M + e^- \rightarrow MH_{ads} \quad \text{(acidic)} \tag{2.1}$$

$$H_2O + M + e^- \rightarrow MH_{ads} + OH^- \quad \text{(alkaline)} \tag{2.2}$$

In the Volmer reaction, hydrogen absorbs on the catalytic material to form a MH_{ads} intermediate, followed by a Heyrovsky reaction or Tafel reaction. In the Heyrovsky reaction, the dihydrogen is formed through an electrochemical desorption:

$$MH_{ads} + H^+ + e^- \rightarrow M + H_2 \quad \text{(acidic)} \tag{2.3}$$

$$MH_{ads} + H_2O + e^- \rightarrow M + OH^- + H_2 \quad \text{(alkaline)} \tag{2.4}$$

The hydrogen can also undergo a chemical desorption process through the Tafel reaction:

$$2\ MH_{ads} \rightarrow 2\ M + H_2 \tag{2.5}$$

The binding energy of hydrogen to the catalyst is the key factor of HER activity. Among the HER catalysts, noble metals such as Pt and Pd have moderate binding energy with hydrogen, thus showing excellent HER activities [25]. However, the high cost and stability issue of Pt catalysts motivate the scientists to find alternative materials for HER.

Here, we summarize the doping effects and synergetic effects of Au NCs in HER. We also introduce how the computational technique is used in these cases to explain differences in catalytic activity and verify proposed mechanisms. These works offer some insights into the catalytic reactions, which is expected to further pave the way for future design of catalyst materials.

2.3.1 Pt or Pd Doped Au_{25} NCs in HER

The study of Au NCs as HER catalysts was reported by Kyuju et al. in 2017 [26]. A molecular-like Pt_1Au_{24} nanocluster was prepared and used as catalysts in homogeneous HER. Following this work, the same group further studied the Pd_1Au_{24}, Pd_2Au_{36} and Pt_2Au_{36} nanoclusters [27]. In the case of Au_{25} nanocluster, the doping atom (Pd or Pt) exclusively replaces the central gold atom in the nanocluster. The

overall structure of nanoclusters remains unchanged after doping, while the mass spectrum and optical absorption spectrum obviously changed (Fig. 2.3). In the mechanistic study of nanoclusters as HER catalysts, Voltammetry was used to study the electron transfer properties (Fig. 2.4). The redox potentials are drastically changed after Pt doping. Also, compared with Au_{25}, Pt_1Au_{24} has more positive onset potential and higher current. Combining the voltammetry and linear weep voltammograms (LSVs) with different concentration of trifluoroacetic acid (TFA), it can be seen that the $[PtAu_{24}]^{1-/2-}$ peak at 1.10 V drastically rises with increasing TFA concentration, indicating that the $[PtAu_{24}]^{2-}$ is the major contributor for enhanced HER activity. Also, the production rate with the Pt_1Au_{24} catalyst is significantly higher than that of the commercial Pt/C catalyst. Additionally, the charge-state-dependent catalytic activity results show that the catalytic currents at potentials negative to the $[PtAu_{24}]^{1-/2-}$ exhibit a linear correlation with $[PtAu_{24}]$ and $[TFA]^{1/2}$, corresponding

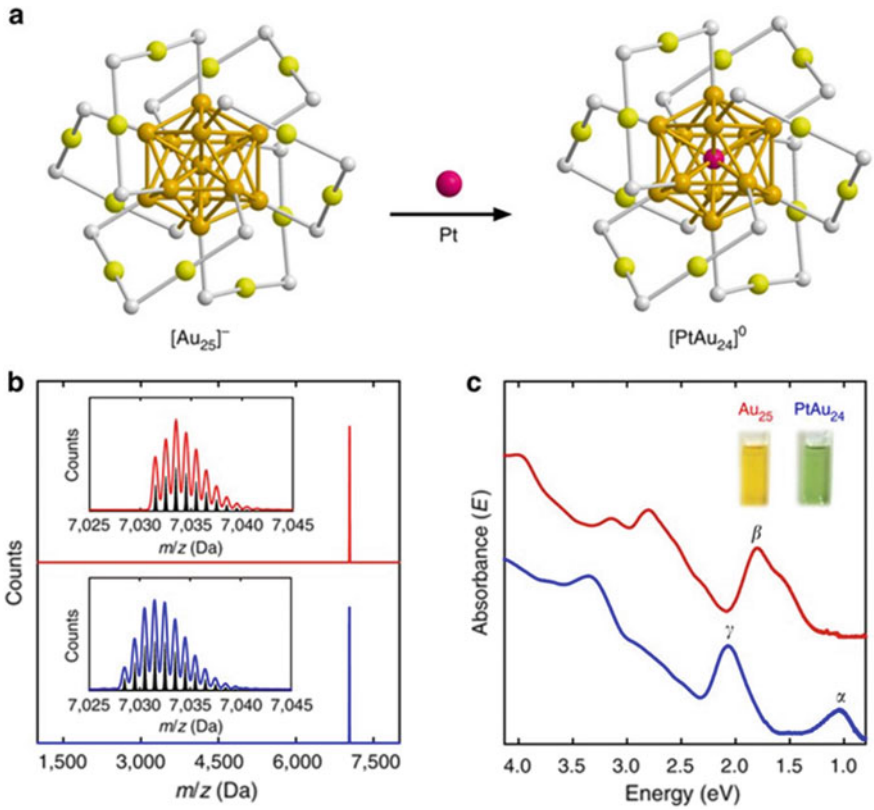

Fig. 2.3 **a** Structures of Au_{25} and $PtAu_{24}$ NCs (golden, Au atoms of the kernel; olive, Au atoms of the shell; gray, sulfur), **b** Mass spectrometry analysis of Au_{25} (red) and Pt_1Au_{24} (blue) NCs, **c** UV-vis-NIR absorption spectra of Au_{25} (red) and Pt_1Au_{24} (blue) NCs. Adapted with permission from Ref. [26]. Copyright 2017 Springer Nature

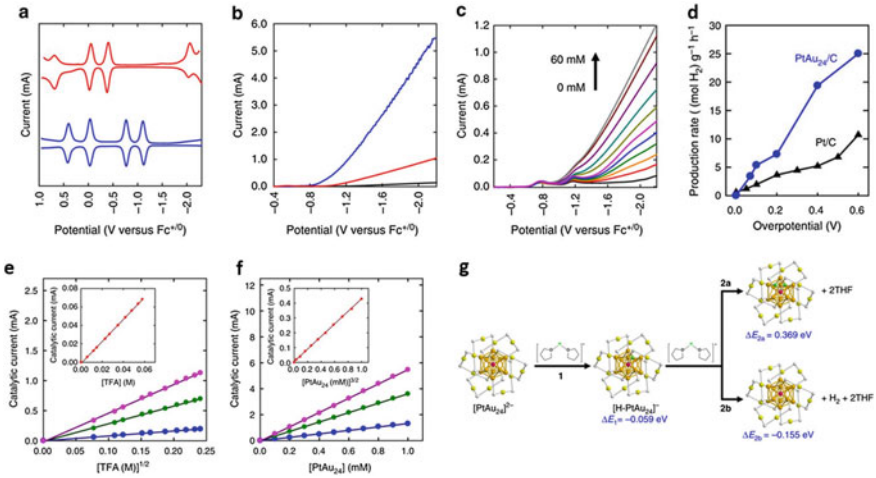

Fig. 2.4 **a** Square-wave voltammetry (SWV) of Au_{25} (red) and $PtAu_{24}$ (blue) NCs, **b** LSV of Au_{25} (red) and $PtAu_{24}$ (blue) NCs, **c** LSVs of $PtAu_{24}$ in THF in the presence of 0. 4. 8, 12, 17, 21, 27, 34, 45, 55, and 60 mM of trifluoroacetic acid (TFA), **d** H_2 production rates per mass of metals in catalyst at various overpotentials on $PtAu_{24}$ (blue) and Pt/C electrodes (red), **e** Dependence of the catalytic current Ic on the concentration of TFA in the presence of $PtAu_{24}$ (I mM), **f** Dependence of the catalytic current Ic on the concentration of $PtAu_{24}$ in TFA (1 M) solution at −1.3 V (blue), −1.8 V (green) and −2.2 V (purple), insets show dependence of the Ic on the concentration of **e** TFA and **f** $PtAu_{24}$ at −1.0 V, **g** calculated reaction energies for HER on $PtAu_{24}$. Adapted with permission from Ref. [26]. Copyright 2017 Springer Nature

to the Volmer–Heyrovsky mechanism [28, 29]. Meanwhile, the currents exhibit a linear correlation with [TFA] and $[PtAu]^{3/2}$ at −1.0 V where $[PtAu_{24}]^{1-}$ is dominant, corresponding to the Volmer–Tafel mechanism [28]. These results are reasonable considering the charge state of Pt_1Au_{24} at different potential. To be specific, the dominant $[PtAu_{24}]^{2-}$ at negative potential adsorbs a proton to form $[H–PtAu_{24}]^{1-}$ with negative charge, which is prone to react with another proton to evolve H_2. On the other hand, the dominant $[PtAu_{24}]^{1-}$ at −1.0 V will form $[H–PtAu_{24}]^{0}$ after adsorbing a proton. Therefore, the Tafel pathway is preferred at this potential.

DFT calculations are also utilized to explain the enhanced catalytic activity of Pt_1Au_{24} (Fig. 2.4g). The results show that the adsorption of the first proton on Pt_1Au_{24} is thermodynamically neutral, while the second proton adsorption is endothermic. This result is consistent with the charge-state-dependent catalytic activity. On the other hand, the geometry optimization shows that the proton is prone to bind with the Pt atom in the icosahedral center. Therefore, the stronger H–Pt interaction with respect to H–Au is a key factor for the enhanced HER activity. Using the same strategies, the group also studied the HER activities of Pd_1Au_{24}, Pt_2Au_{36} and Pd_2Au_{36} [27]. These works proved the versatility of metal NCs in catalytic mechanism study. Especially, the introduction of SWV and DFT calculation makes the metal NCs a perfect tool to correlate the structure and properties.

2.3.2 Boosting HER Activity with Au NCs/MoS_2 Composite

Besides the doping effects, metal NCs are also reported to show strong synergetic effects when loaded on other materials. In 2017, the synergetic effect was reported by Zhao et al. [30]. In this work, $Au_{25}(SR)_{18}$ and $Au_{25}(SePh)_{18}$ NCs are loaded on the MoS_2 ultra-thin nanosheets. These two NCs have a similar kernel structure but different protecting ligands. The TEM images and XPS spectra indicate the successful loading of Au NCs on the surface of MoS_2 (Fig. 2.5). The Mo 3d XPS of composites exhibits negative shifting compared with MoS_2, while the Au 4f spectra of composites show obvious positive shifting compared with Au_{25} NCs. The XPS results clearly indicate that the electron density transfers from Au_{25} to MoS_2. In the HER activity test, the thiolate-protected Au_{25} NCs exhibit a more positive onset potential and higher current density compared with MoS_2 nanosheets. On the other hand, the benzeneselenolate-protected Au_{25} NCs loaded MoS_2 nanosheets show similar synergetic effects. However, the enhancement is less obvious compared with the thiolate-protected Au_{25} NCs. To explain the different enhancement in HER catalytic activity, Au 4f XPS spectra of $Au_{25}(SR)_{18}/MoS_2$, $Au_{25}(SePh)_{18}/MoS_2$ and pure MoS_2 are obtained. The $Au_{25}(SR)_{18}/MoS_2$ composites exhibit more positive shifting compared with the $Au_{25}(SePh)_{18}/MoS_2$ composites, indicating stronger electron density transfer effects of thiol protected Au_{25}. Therefore, the electron interaction between MoS_2 nanosheets and Au NCs is a key factor for the HER activity. Based on these results, the authors proposed a dual interfacial effect, where the core/ligand interface of Au NCs and the MoS_2/Au NCs interface are both important in the HER catalytic activity.

Du et al. also studied the synergetic effects between Au_2Pd_6 NCs and MoS_2 [31]. In this work, DFT calculation is used to investigate the origin of the enhanced HER activity. The DFT calculation shows the $_{\Delta}G$ for a proton adsorbed at Au_2Pd_6/MoS_2 composite is more negative than that of MoS_2, indicating better HER activity of the composites. Besides, it is found that in the Au_2Pd_6 composites, both Au atoms and S atoms have appropriate $_{\Delta}G$ for proton adsorption. In contrast, only the Au–Pd bridge site has proper $_{\Delta}G$ in Au_2Pd_6 NCs, and no proper active site for proton adsorption can be found in defect-free MoS_2. Therefore, the significant increase in active sites in the composites is a key factor for boosted HER activity. Meanwhile, the DOS analysis also explained the enhanced activity of composites. The Au_2Pd_6 composites have a defect state near the Fermi level. This unique defect state narrows the band gap, leading to a better electronic conductivity.

2.4 Oxygen Evolution Reaction with Metal NCs

Oxygen evolution reaction (OER) is the other half reaction in water splitting and is indeed critical. Oxygen can be formed through several proton/electron-coupled steps in OER. The reaction can be described as follows:

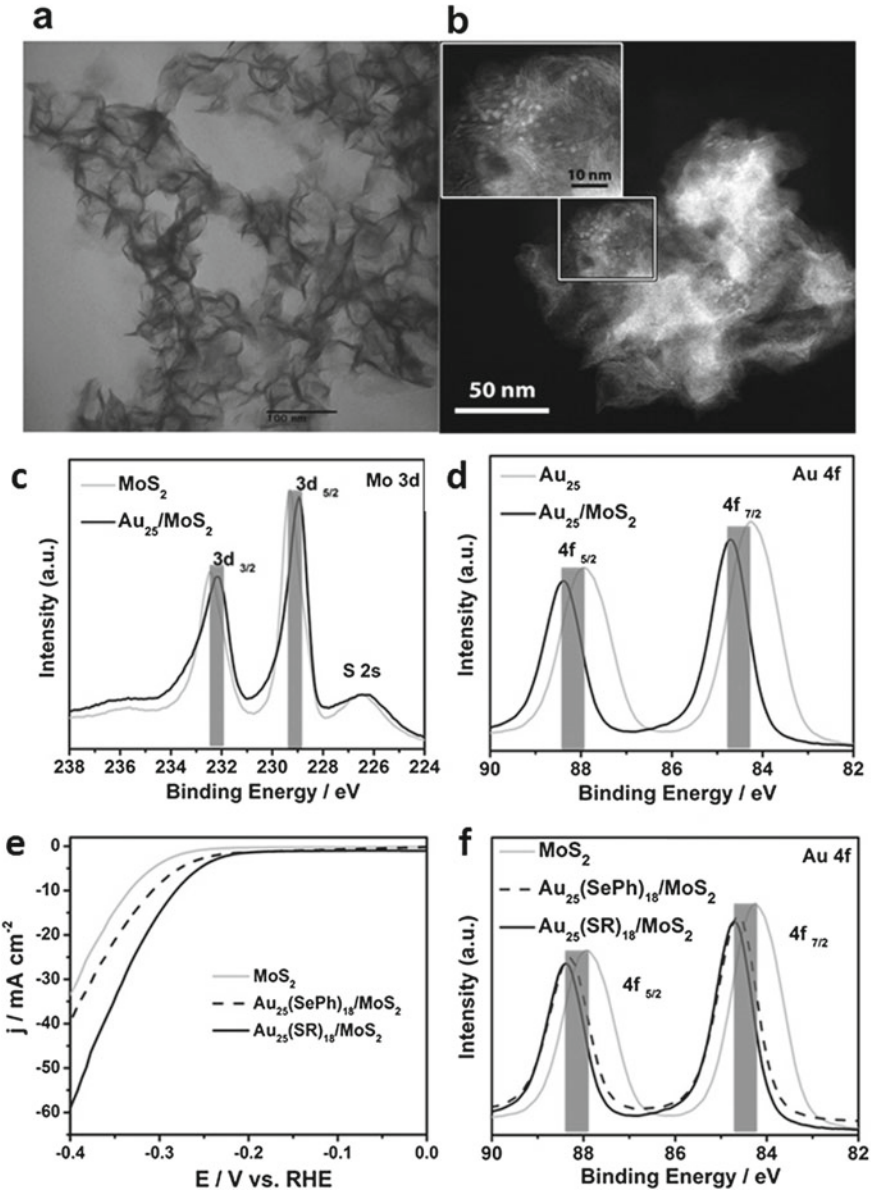

Fig. 2.5 **a** TEM image of the MoS_2 nanosheets, **b** HAADF-STEM image of the Au_{25}/MoS_2 composite, **c** high-resolution Mo 3d XPS spectra of MoS_2 nanosheet and Au_{25}/MoS_2 composite, **d** high-resolution Au 4f XPS spectra of Au_{25} NCs and Au_{25}/MoS_2 composite, **e** HER LSV curves, **f** high-resolution Au 4f XPS spectra of MoS_2, $Au_{25}(SePh)_{18}/MoS_2$ and $Au_{25}(SR)_{18}/MoS_2$ composite. Adapted from Ref. [30]. Copyright 2017 Wiley-VCH

$$2\ H_2O \rightarrow 4\ H^+ + O_2 + 4\ e^- \quad \text{(acidic)} \tag{2.6}$$

$$4\ OH^- \rightarrow 2\ H_2O + O_2 + 4\ e^- \quad \text{(alkaline)} \tag{2.7}$$

In OER, the formation of oxygen requires a four-electron transfer, and the reaction kinetically favors single electron transfer at each step [32]. Therefore, catalysts are required to overcome the energy barrier and lower the high overpotential in the sluggish OER [33, 34]. To reduce the cost of catalyst materials, cheaper and efficient alternative catalytic materials are extensively studied to replace the current Ir-based materials. In previous reports, anchoring a small amount of gold onto cobalt-based materials can enhance the OER activity [35, 36]. However, the mechanism for the improvement was not well understood due to the variability and complicacy of the gold-loaded composites. In this section, the synergetic effects between Au NCs and $CoSe_2$ nanosheets are introduced. This unique composite may provide valuable insights into the mechanistic study by taking advantage of the precise atomic structures of Au NCs [1].

2.4.1 Au_n NCs Promote OER at the Nanocluster/$CoSe_2$ Interface

The OER performance of metal NCs was first reported by Zhao et al. in 2017 [37]. In this work, composites of Au_{25} and ultra-thin $CoSe_2$ nanosheets were synthesized and tested as OER catalysts. TEM images clearly show the ultra-thin nanosheet structure of $CoSe_2$ (Fig. 2.6a–c). In the high-angle annular dark field scanning transmission electron microscopy (HAADF-STEM), it can be observed that Au nanoclusters are homogeneously dispersed on the surface of $CoSe_2$ nanosheets.

In the electrochemical test (Fig. 2.6d–f), the $Au_{25}/CoSe_2$ composites show much smaller onset potential (1.406 V vs. RHE) and higher current density than $CoSe_2$ nanosheets and Au_{25}-loaded carbon. At 1.68 V, $Au_{25}/CoSe_2$ composites achieve a current density of 11.78 mA cm^{-2}, which is 2.4 times that of $CoSe_2$ nanosheets (4.92 mA cm^{-2}) and 20.7 times that of Au_{25}-loaded carbon (0.57 mA cm^{-2}). Also, the composites exhibit higher current density and smaller overpotential than commercial Pt/C catalysts. In the stability test, the polarization curve and UV-vis spectra of the $Au_{25}/CoSe_2$ composites exhibit the same features before and after 1000 cycles, indicating excellent stability of the composites as OER catalysts (Fig. 2.6g).

The XPS and Raman analysis of $CoSe_2$ and composites were conducted to explain the enhanced OER activity of $Au_{25}/CoSe_2$ composites (Fig. 2.7). The binding energy of Co 2p in the composites shows a ~1 eV decrease compared with $CoSe_2$, indicating electronic interaction between the Au_{25} and $CoSe_2$ nanosheet. Also, the Raman peak at ca. 657 cm^{-1} exhibits a shift toward higher wavenumber, suggesting the electronic interaction. It is believed that such an electronic interaction is a key factor that stabilizes the hydroperoxyl intermediates and optimizes interaction between $CoSe_2$ and oxygen.

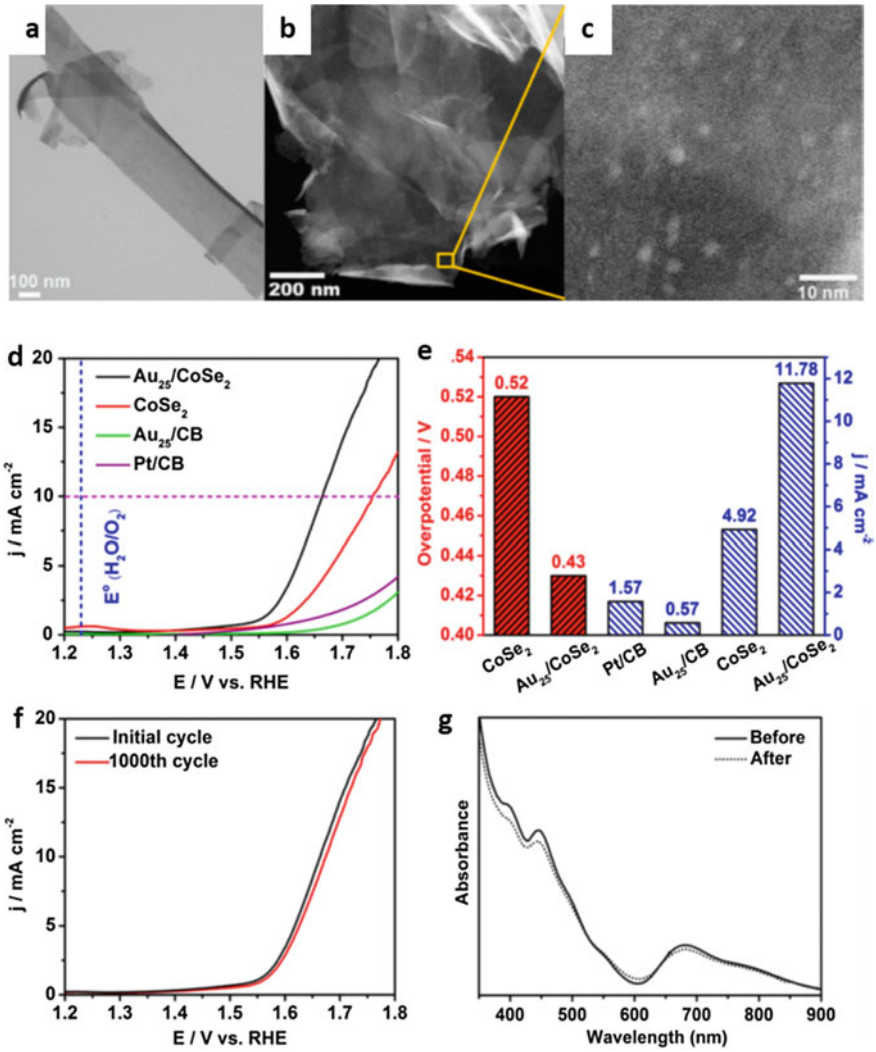

Fig. 2.6 **a** TEM image of $CoSe_2$ nanosheets, **b**, **c** HAADF-STEM images of $Au_{25}/CoSe_2$ composite, **d** OER polarization curves of $Au_{25}/CoSe_2$, $CoSe_2$, Pt/C and Au_{25}/C, **e** overpotential at the current density of 10 mA cm^{-2}, and the current density at the overpotential of 0.45 V for $Au_{25}/CoSe_2$, $CoSe_2$, Pt/C and Au_{25}/C catalysts, **f** stability test of $Au_{25}/CoSe_2$,HER LSV curves, **g** UV-vis spectra of Au_{25} NCs before and after the stability test. Adapted from Ref. [37]. Copyright 2017 American Chemical Society

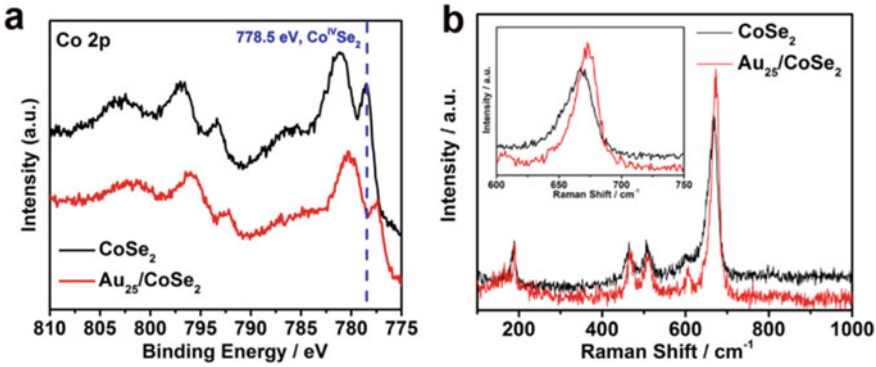

Fig. 2.7 **a** High-resolution Co 2p XPS spectra of $CoSe_2$ and $Au_{25}/CoSe_2$ composites, **b** Raman spectra of $CoSe_2$ and $Au_{25}/CoSe_2$ composites. Adapted from Ref. [37]. Copyright 2017 American Chemical Society

2.4.2 Au_n NC Size Effect in OER

The size of gold nanoclusters is also important for the catalytic activity. To study the potential size dependence of Au_n NCs for OER, Zhao et al. compared gold nanoclusters of $Au_{10}(SPh\text{-}^tBu)_{10}$, $Au_{25}(SR)_{18}$, $Au_{144}(SR)_{60}$ and $Au_{333}(SR)_{79}$, with the latter three being protected by the same phenylethanethiolate ligand. These NCs were loaded onto $CoSe_2$ (all at 2.0 wt%, denoted as $Au_n/CoSe_2$). The OER polarization curves show a moderate increase of OER activity with an increase in cluster size. The $Au_{333}/CoSe_2$ catalyst possesses the smallest overpotential (~0.41 V for 10 mA cm^{-2}) and the largest current density (15.44 mA cm^{-2} at the overpotential of 0.45 V).

2.5 Oxygen Reduction Reaction with Au NCs

The ORR is the rate-determining step of the fuel cell system because of its sluggish kinetics [38, 39]. In both acidic and alkaline electrolyte, different mechanisms have been documented for ORR. These processes can be described as follows:

$$\text{Acidic:}\quad O_2 + 4\,H^+ + 4\,e^- \rightarrow 2\,H_2O \tag{2.8}$$

$$O_2 + 2\,H^+ + 2\,e^- \rightarrow H_2O_2 \tag{2.9}$$

$$H_2O_2 + 2\,H + 2\,e^- \rightarrow 2\,H_2O \tag{2.10}$$

$$\text{Alkaline:}\quad O_2 + H_2O + 4\,e^- \rightarrow 4\,OH^- \tag{2.11}$$

$$O_2 + H_2O + 2\,e^- \rightarrow HO_2{}^- + OH^- \tag{2.12}$$

$$HO_{2^-} + H_2O + 2\,e^- \rightarrow 3\,OH^- \tag{2.13}$$

From the equations, it can be seen that two possible pathways can be observed in ORR in both electrolytes. One of them is the direct $4e^-$ pathway where oxygen is reduced to H_2O in acidic electrolytes or OH^- in alkaline electrolytes. The other pathway is the $2e^-$ mechanism where H_2O_2 or $HO_2{}^-$ is first formed before the sequent reduction to H_2O or OH^- with another $2e^-$ transfer. It is believed that the commercial Pt/C electrode favors the direct $4e^-$ pathways. However, the complicated surface structure of Pt/C catalysts makes it challenging to figure out the reaction occurring in the catalytic process [40–42]. To understand the ORR mechanism, several noble metal nanoparticle-based catalytic materials with either direct $4e^-$ or $2e^-$ pathways have been extensively studied [43–49]. Among these catalysts, Au has shown several unique properties in ORR. In 2007, Zhang et al. found that Pt catalysts can be stabilized against dissolution by modification with Au NCs [50]. In their electrochemical study, the Au NCs-modified Pt catalysts exhibit ultra-high stability where the polarization curve remains unchanged after 30,000 cycles. Later, Yin et al. reported in 2012 the Au NCs/graphene hybrids for high-performance ORR [51]. The hybrid catalytic materials exhibit high current density and excellent stability comparable to that of the commercial Pt/C catalysts. Yet, no study about combining the atomically precise Au NCs with DFT calculations is reported. The precise structure and ultra-small size make the Au NCs a perfect system to study the size effect in ORR. In this section, the reports on the size effects of atomically precise Au NCs are introduced.

2.5.1 Nanocluster-Derived Ultra-Small Nanoparticles for ORR

The size effect has been extensively studied for Au nanoparticles in the past decades [52, 53]. However, reports are rare for ultra-small Au nanoparticles (i.e., core diameter <2 nm) for ORR. In 2016, Wang et al. reported porous carbon-supported ultra-small nanoparticles as ORR catalysts using thiolate-capped Au_{25}, Au_{38} and Au_{144} NCs as precursors [54]. The average diameters of Au nanoparticles were estimated to be 3.7 $\pm$ 0.9 nm for Au_{25}-derived catalyst (AuPC-1), 4.9 $\pm$ 1.1 nm for Au_{38}-derived one (AuPC-2), and 5.8 $\pm$ 1.25 nm for Au_{144}-derived one (AuPC-3), as shown in Fig. 2.8. All the Au nanoparticles are larger than the sizes of the original nanoclusters because of aggregation of clusters during the calcination.

In the electrochemical test (Fig. 2.9), it is found that the AuPC-1 sample exhibits a peak current density similar to that of commercial Pt/C (0.57 mA cm^{-2}). The rotation ring and disk electrode (RRDE) measurements show that the onset potential is 0.95, 0.91, and 0.89 V for AuPC-1, AuPC-2, and AuPC-3, respectively. Also, the diffusion-limited current density of AuPC-1 (3.61 mA cm^{-2}) is obviously higher than

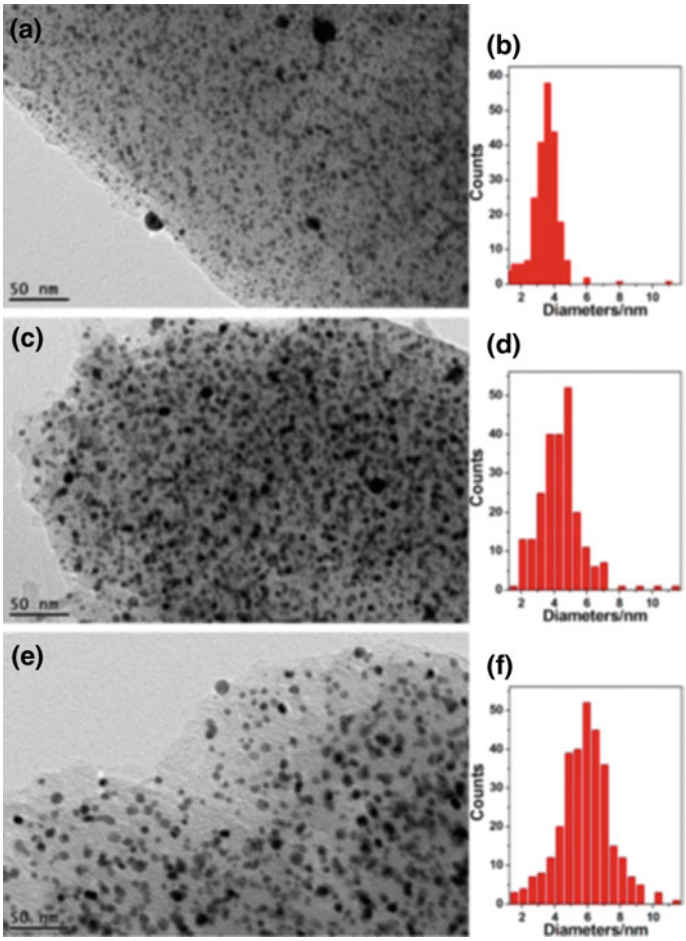

Fig. 2.8 TEM images of **a** AuPC-1, **c** AuPC-2, and **e** AuPC-3, with the corresponding size distribution in panels **b**, **d**, and **e**. Adapted with permission from Ref. [54]. Copyright 2016 American Chemical Society

that of AuPC-2 (3.21 mA cm^{-1}) and AuPC-3 (3.16 mA cm^{-2}). It is noted that the ORR activity of AuPC-1 is similar to that of the commercial Pt/C catalysts (0.95 V for onset potential and 4.98 mA cm^{-2} for limiting current density). Taking all the results together, one can find that the ORR activity increases with the decreasing Au nanoparticle size. Especially, the smallest AuPC-1 sample shows a comparable activity with the commercial Pt/C electrode.

In the Tafel plots (Fig. 2.9c), it can be seen that the specific activity increases with the decrease of AuPC nanoparticle size. At 0.8 V, the current density increases in the order of AuPC-3 (0.16 mA cm^{-2}) < AuPC-2 (0.195 mA cm^{-2}) < AuPC-1 (0.612 mA cm^{-2}) < commercial Pt/C (0.615 mA cm^{-2}). Additionally, similar

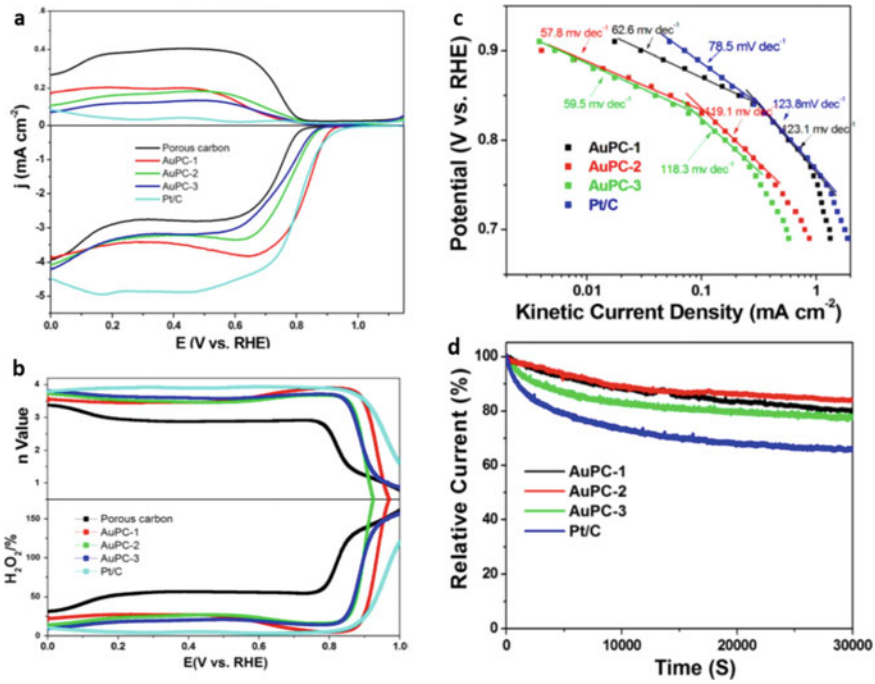

Fig. 2.9 **a** CV curves, **b** the ORR polarization curves, **c** Tafel plots, **d** Chronoamperometric profiles of AuPC-1, AuPC-2, AuPC-3 and Pt/C catalysts. Adapted with permission from Ref. [54]. Copyright 2016 American Chemical Society

features of the Tafel plots can be observed for all the catalysts. Two clear linear regions are displayed at low and high overpotentials. In the low overpotential region, the slopes of these catalysts are all close to 60 mV dec^{-1}, indicating that a pseudo-two-electron reaction might be the rate-determining step. However, the similar slopes of approximately 120 mV dec^{-1} for the four catalysts suggest that the rate-determining step is probably the first electron transfer to oxygen molecules. Also, the stability test of AuPC and commercial Pt/C catalysts indicate superior stability of Au nanoparticles in ORR. The relative current of AuPC-1, AuPC-2, and AuPC-3 shows a loss of 19.2%, 15.6%, and 22.7%, respectively, after 8 h. While for commercial Pt/C catalysts 35% loss of current is observed. The authors ascribe the superior performance of nanoclusters-derived ultra-small nanoparticles to the low-coordination surface Au atoms of small-sized nanoparticles and the synergetic effects between carbon and Au.

In summary, the small-sized Au particles are beneficial for the activation of oxygen, thus increasing the catalytic activity of ORR.

2.5.2 Size Effect of Au NCs in ORR

Au NCs were first reported for ORR by Chen et al. in 2009 [55]. Four Au NCs with different sizes: Au_{11}, $Au_{\sim 25}$, $Au_{\sim 55}$, and $Au_{\sim 140}$ are synthesized. (On a note, we found that the UV-vis spectrum of "Au_{11}" [55] instead resembles that of the Au_{25} rod cluster [1]). In the electrochemical test, it was found that the "Au_{11}" exhibits the highest limiting current density and smallest overpotential in ORR. Overall, the catalytic activity decreases as the cluster size increases. However, the crystal structures of Au NCs were not obtained at that time. Therefore, the assignment of precise atom numbers was preliminary. Later, Jones et al. reported in 2018 a series of t-butylthiolate protected Au NCs with increasing sizes for ORR [56]. These four nanoclusters, namely Au_{23}, Au_{30}, Au_{46}, and Au_{65}, show distinct UV-vis spectra as shown in Fig. 2.10, and different colors were observed for these four nanoclusters. The same t-butylthiolate ligand and different core sizes make it ideal to compare the atomically precise size effect with this series of Au NCs.

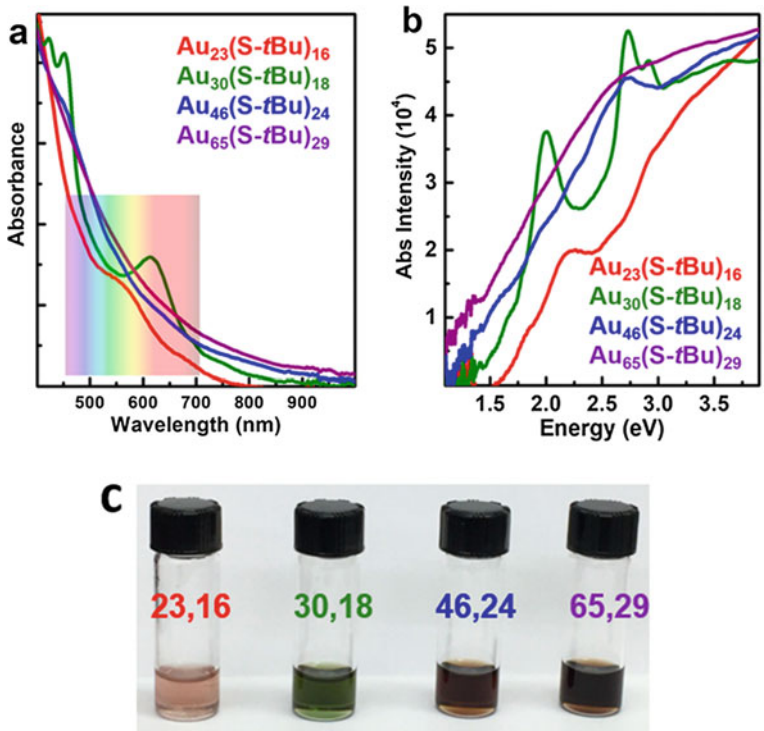

Fig. 2.10 **a** UV-vis spectra, **b** photon energy plot (eV), and **c** photograph of Au_{23}, Au_{30}, Au_{46} and Au_{65}. Adapted with permission from Ref. [56]. Copyright 2018 American Chemical Society

Table 2.1 Experimental parameters for Au NC-catalyzed ORR (n: the number of transferred electrons)

Sample	$\eta(V)$ at $j = -1$ mA cm^{-2}	n	HO^- (%)
Au_{23}/SWNT	0.68	2.1	53
Au_{30}/SWNT	0.25	2.5	63
Au_{46}/SWNT	0.24	2.0	50
Au_{65}/SWNT	0.08	3.2	80

Data from Ref. [56]

In the electrochemical test (Table 2.1), the Au_{65} exhibits a transfer of 3.2 electrons, which is higher than that of other NCs (approximately 2 electrons). Also, the potential at -1 mA cm^{-2} shows a trend of $Au_{65} < Au_{46} < Au_{30} < Au_{23}$, indicating that the ORR catalytic activity increases as the nanocluster size grows. Therefore, it can be concluded that larger NCs can facilitate the ORR with smaller overpotential, higher diffusion-limiting current and higher selectivity toward OH^- production.

2.5.3 Charge-State-Dependent ORR Activity of Au_{25} NCs

In 2007, Negishi et al. reported the charge state of Au_{25} NCs can be tuned between -1, 0 and $+1$ [57]. This unique property provides an ideal model to study the charge-state effect of Au NCs in electrochemical catalysis [58–60]. Later in 2014, Lu et al. synthesized these atomically precise Au_{25} NCs protected by dodecanethiolate with different charge states (-1, 0 and $+1$) for ORR [61]. The UV-vis spectra clearly show the different features of the as-prepared NCs. In addition, the Au $4f_{7/2}$ binding energy shows a positive shift when the charge state becomes more positive, further indicating the different charge state of Au_{25} NCs (Fig. 2.11).

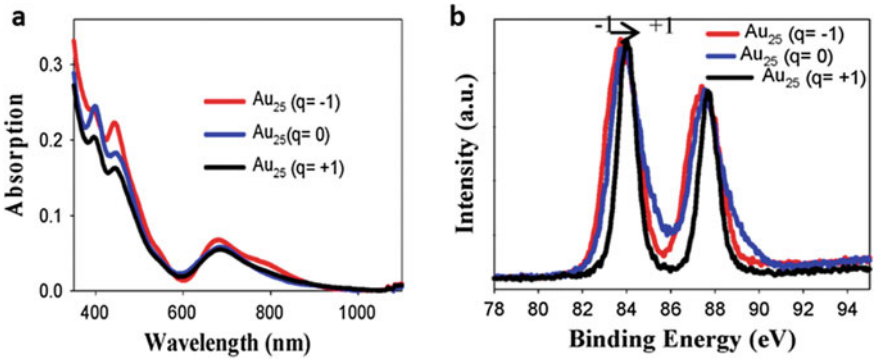

Fig. 2.11 **a** UV-vis spectra and **b** XPS spectra of Au_{25} NCs with different charge states. Adapted with permission from Ref. [61]. Copyright 2014 Royal Society of Chemistry

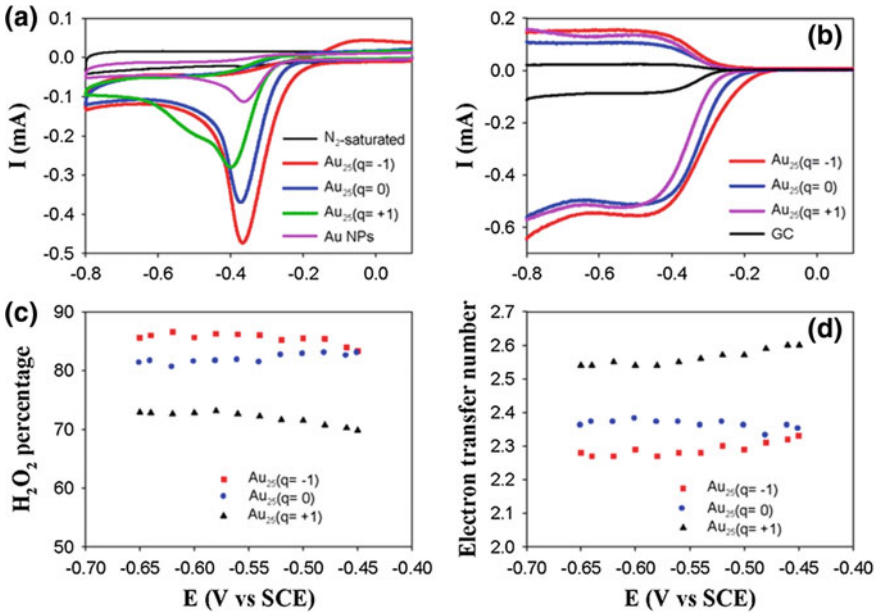

Fig. 2.12 **a** CV of the ORR on Au nanoparticles and Au_{25} NCs with different charge states, **b** RRDE voltammograms recorded on glass carbon electrode and the Au_{25} NCs, **c** selectivity of the H_2O_2, **d** the electron transfer number as a function of the applied potentials. Adapted with permission from Ref. [61]. Copyright 2014 Royal Society of Chemistry

The electrochemical test results show that the Au_{25}^- shows a more positive onset potential and higher diffusion-limiting current density compared with Au_{25}^0 and Au_{25}^+ (Fig. 2.12). Also, the H_2O_2 production percentages show a trend of Au_{25}^- (86%) > Au_{25}^0 (82) > Au_{25}^+ (72%), indicating that the two-electron pathway is dominant with the Au_{25} nanoclusters. Thus, the Au_{25}^- can be used as a promising catalyst for H_2O_2 production in ORR. The combined experimental results and previous DFT calculations suggest that charging the cluster can increase the chemical activity with respect to O_2 [62]; the authors proposed that the strong charge-state effects on H_2O_2 production can be attributed to electron transfer from the anionic Au_{25} core into the LUMO (π^*) of O_2, activating the O_2 molecule and generating peroxo-like species.

2.6 CO_2 Reduction Reaction with Metal NCs

CO_2 reduction reaction (CO_2RR) has been extensively investigated in order to remediate the global climate change issues during the past decades. As a multiproton and multi-electron process, the CO_2 RR is a complicated process with several products produced at various voltages as shown in Table 2.2 [63]. Especially, the formation of CO_2^- key intermediate consumes a large amount of energy. On the other hand, the

Table 2.2 Reduction potentials (vs. RHE) of various products in CO_2 reduction reactions

Product	Reaction	E^0 [V vs. RHE]
CO	$CO_2 + 2\,e^- + 2\,H^+ \rightarrow CO + H_2O$	−0.11
HCOOH	$CO_2 + 2\,e^- + 2\,H^+ \rightarrow HCOOH$	−0.25
HCOH	$CO_2 + 4\,e^- + 4\,H^+ \rightarrow HCOH + H_2O$	−0.07
CH_3OH	$CO_2 + 6\,e^- + 6\,H^+ \rightarrow CH_3OH + H_2O$	0.02
CH_4	$CO_2 + 8\,e^- + 8\,H^+ \rightarrow CH_4 + 2\,H_2O$	0.17
C_2H_4	$2\,CO_2 + 12\,e^- + 12\,H^+ \rightarrow C_2H_4 + 4\,H_2O$	0.06
CO_2^-	$CO_2 + e^- \rightarrow CO_2^{\cdot-}$	−1.5
H_2	$2\,H^+ + 2\,e^- \rightarrow H_2$	0.0

Data adapted from Ref. [63]

competing HER also hinders the efficient CO_2RR in aqueous solutions. Therefore, highly efficient catalysts are critically required to lower the energy barrier in CO_2RR [64–66].

Among the catalytic materials, Au has been extensively studied due to its high selectivity toward CO formation [14]. On the other hand, Cu is also attractive because of its versatility in forming various hydrocarbon products [67]. In this section, we summarize the Au and Cu NCs as catalysts for CO_2RR. The application of atomically precise NCs offers an opportunity for correlating the structure and catalytic properties, hence providing insights into the mechanism and also fundamental rules for future design of advanced catalytic materials for CO_2RR.

2.6.1 Au_{25} for CO_2RR

In 2012, Kauffman et al. first reported atomically precise Au_{25} NCs as catalysts for CO_2RR [68]. The electrochemical results show that Au_{25} have much higher activity in CO_2RR than Au nanoparticles and bulk Au as shown in Fig. 2.13. To be detailed, the Au_{25} exhibits higher current density in LSV and higher CO formation rate than Au nanoparticles and bulk Au.

To explain the superior activity of the Au_{25} nanocluster, the same group used DFT calculations to obtain the free energy diagram of the CO_2RR process (Fig. 2.14) [69]. They proposed that partial ligand removal would occur in order to expose the active sites for CO_2 adsorption. The free energy diagrams of both fully ligand-protected Au_{25} and singly dethiolated Au_{25} cluster were obtained. In the energy diagrams, it can be seen that the most endergonic step for both cases is the *COOH formation. The U_{onset} for fully ligand-protected Au_{25} is −2.04 V, much larger than that of singly dethiolated Au_{25} cluster (−0.34 V) and experimentally value (−0.193 V), indicating that their proposal of ligand removal is correct. Therefore, they concluded that the cluster can facilitate the reduction of CO_2 by partial removal of the thiolate ligand.

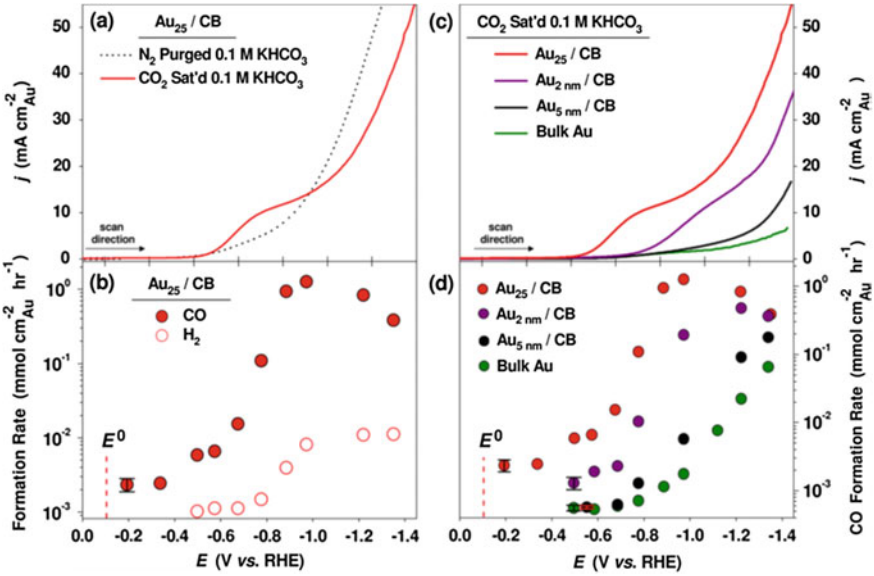

Fig. 2.13 **a** LSV of Au_{25}/CB, **b** potential-dependent H_2 and CO formation rates for Au_{25}/CB, **c** LSV of various Au catalysts in quiescent CO_2 saturated 0.1 M $KHCO_3$, **d** potential-dependent CO formation rates for the various Au catalysts. Adapted from Ref. [68]. Copyright 2018 American Chemical Society

The exposed Au site can reduce the free energy of the COOH intermediate formation, thus lowering the overpotential for CO formation. This group also reported the long-term stability of Au_{25} NCs in CO_2RR. The results show that Au_{25} can catalyze the CO_2RR for 6 days with steady production rate of 745 ± 59 L/(g_{Au} h) and CO selectivity of 86 ± 5%, indicating the exceptional stability of Au_{25} NCs in CO_2RR [70].

2.6.2 Atomic-Level Morphology Effects in CO_2RR

Previously, Au nanomaterials with different morphology have been extensively studied in testing the catalytic activity of facet, edge, and corner. Despite some interesting results, the nonavailable atomic-level structure of these nanomaterials made it difficult to connect the structure and the catalytic properties. To find more solid evidence of morphology effects of Au catalysts in CO_2RR, Zhao et al. prepared atomically precise Au_{25} nanosphere and nanorod and tested their electrochemical performance as CO_2RR catalysts [71]. These two NCs exhibit distinct features in UV-vis spectra, corresponding to their spectroscopic fingerprints (Fig. 2.15). The Au_{25} nanosphere comprises an icosahedral Au_{13} core protected by six dimeric surface staples (–SR–Au–SR–Au–SR–), showing a spherical morphology; while the Au_{25}

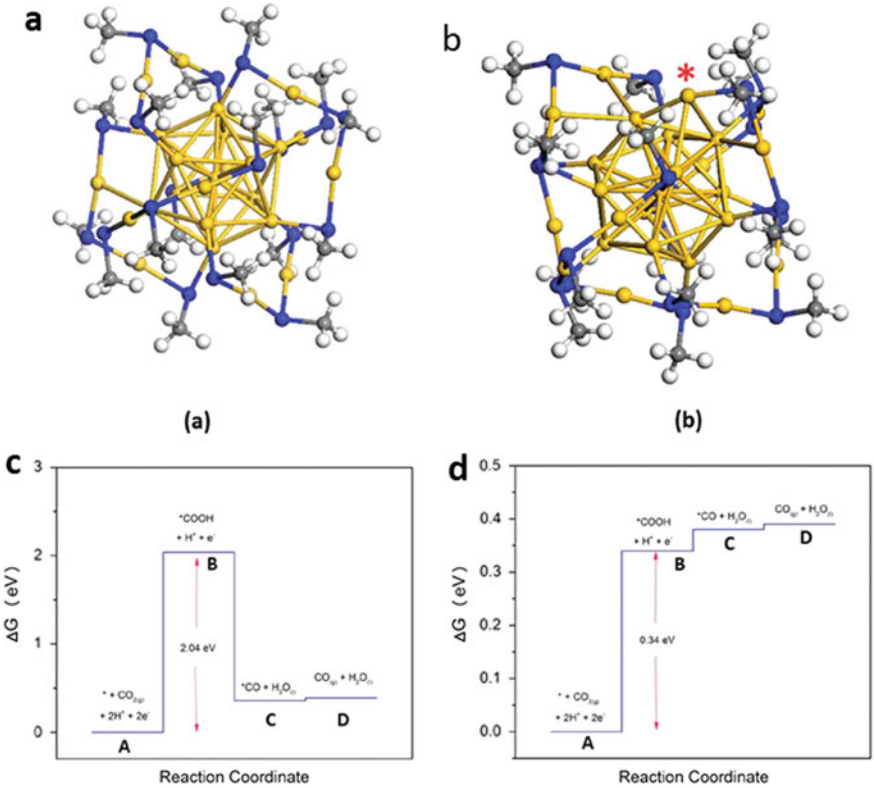

Fig. 2.14 Optimized structure of the model: **a** fully ligand-protected $Au_{25}(SCH_3)_{18}^{-}$ NC and **b** singly dethiolated $Au_{25}(SCH_3)_{17}^{-}$ NC. Free energy diagram for electrochemical reduction of CO_2 to CO: **c** over the fully ligand-protected $Au_{25}(SCH_3)_{18}^{-}$ NC, and **d** over the singly dethiolated $Au_{25}(SCH_3)_{17}^{-}$ NC. White, gray, blue and golden balls represent H, C, S, and Au atom, respectively. Adapted from Ref. [69]. Copyright 2016 the American Institute of Physics

nanorod comprises two Au_{13} icosahedra fused together by sharing one vertex gold atom, and the rod is protected by five bridging thiolates (–SR–) at the rod's waist, 5 phosphine ligands and one chloride on each end of the nanorod.

The electrochemical results in Fig. 2.16 show that Au_{25} nanosphere has higher CO Faradaic efficiency around 70% than the Au_{25} nanorod (30–60%). The Au_{25} nanosphere also exhibits a much higher CO formation rate. Especially, at high potential of −1.17 V, the CO formation rate of Au_{25} sphere (33.3 μL min^{-1}) is 2.8 times that of Au_{25} nanorod (11.7 μL min^{-1}). The larger CO FE and higher CO formation rate of the Au_{25} nanosphere indicate its high catalytic performance compared with the Au_{25} nanorod.

DFT calculations are used to evaluate the free energy of reaction steps to understand the mechanism of the better performance of the Au_{25} nanosphere (Fig. 2.17). First, the $_{\Delta}G$ values for ligand removal from NCs are calculated. For the Au_{25}

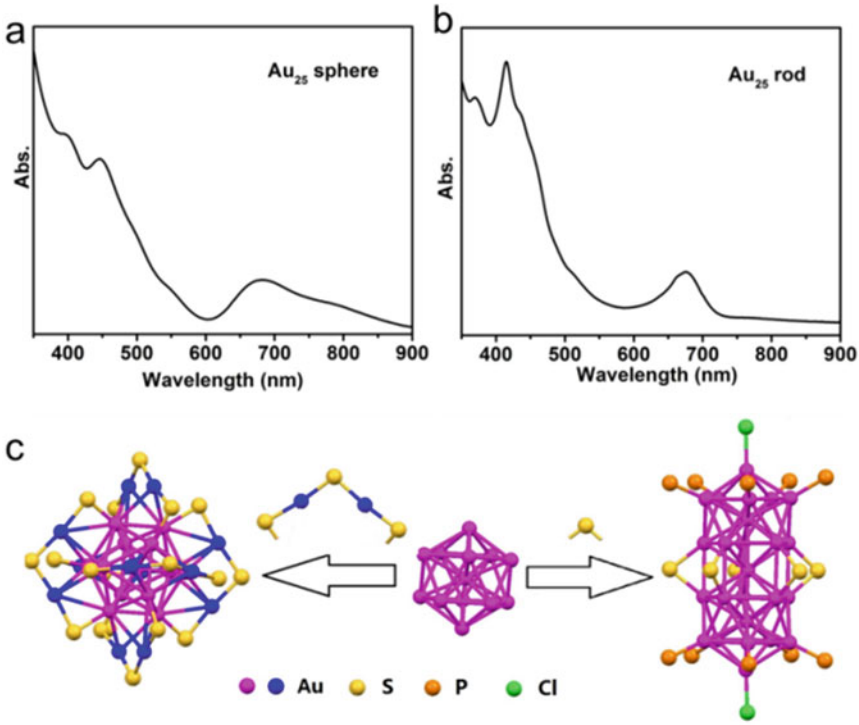

Fig. 2.15 UV-vis spectra of: **a** Au_{25} nanosphere and **b** Au_{25} nanorod; **c** Atom packing structures of Au_{25} nanosphere and nanorod. Adapted from Ref. [71]. Copyright 2018 American Chemical Society

nanosphere, removal of a single $–SCH_3$ is considered, while for the nanorod, removal of $–SCH_3$, –Cl and PH_3 is calculated. The results show that the desorption of $–PH_3$ and the removal of –Cl from the Au_{25} nanorod have the same $_{\Delta}G$: 0.54 eV. For the $–SCH_3$ removal energy of the nanosphere and the nanorod, $_{\Delta}G$ is calculated to be 0.49 eV and 0.95 eV, respectively. These results indicate that the removal of $–PH_3$ and –Cl is more favored for the nanorod. However, the ligand removal from the nanosphere is less endergonic than that from the nanorod. The free energy diagram after ligand removal shows that $^{*}COOH$, an important intermediate in CO_2 reduction to CO on Au, is more stabilized on the $Au_{25}(SCH_3)_{17}$ nanosphere with one $–SCH_3$ ligand removed compared with any of the other ligand-removed systems of the nanorod. Therefore, it is concluded that the energetically favorable removal of $–SCH_3$ from the Au_{25} nanosphere to expose active sites and the stabilization of $^{*}COOH$ intermediates on the obtained $Au_{25}(SCH_3)_{17}$ nanosphere contribute to the superior catalytic performance of the Au_{25} nanosphere. This work has successfully correlated the atomic-level morphology with catalytic performance, explaining the factors that determine the CO_2RR activities with the aid of DFT calculations. It has shed light on the mechanism for the CO_2RR in the future.

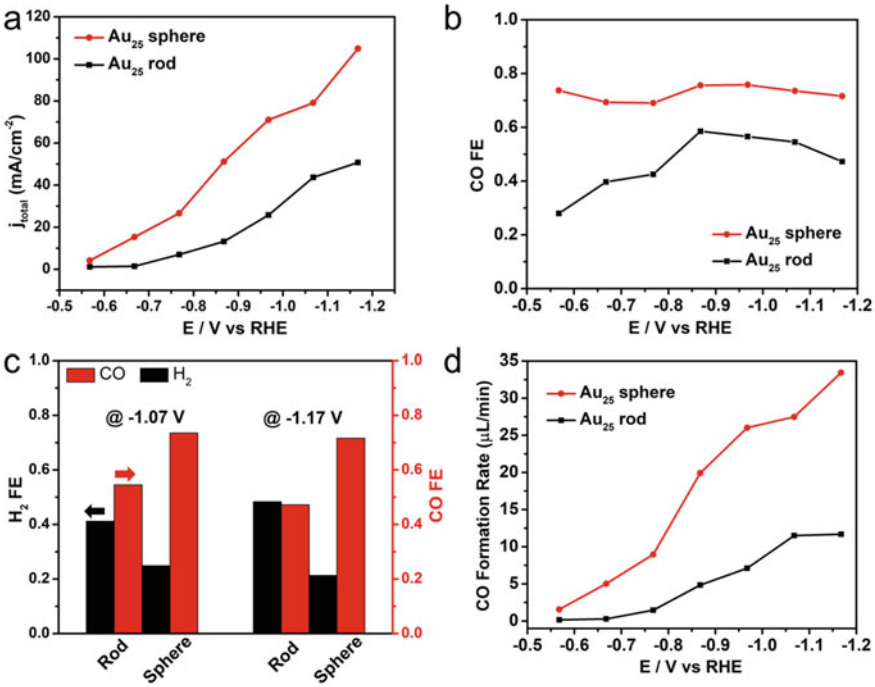

Fig. 2.16 **a** Total current density of CO_2 reduction and **b** Faradaic efficiency (FE) for CO production over the Au_{25} nanosphere and nanorod; **c** FE for CO and H_2 at the potential of −1.07 and −1.17 V over Au_{25} nanosphere and nanorod, **d** CO formation rates over Au_{25} nanosphere and nanorod. Adapted from Ref. [71]. Copyright 2018 American Chemical Society

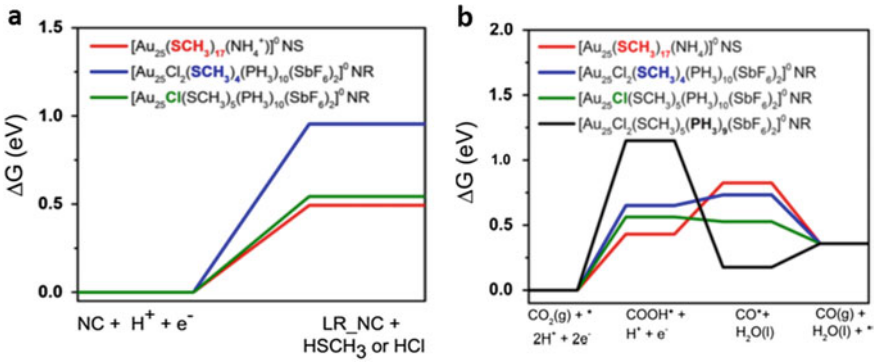

Fig. 2.17 **a** ΔG for ligand removal (eV) from the NCs at 0 V versus RHE, **b** free energy diagrams for CO_2 reduction to CO on the ligand-removed NCs at 0 V versus RHE. Adapted from Ref. [71]. Copyright 2018 American Chemical Society

2.6.3 Cu NC-Catalyzed CO_2RR

Cu catalysts are attractive for their ability to reduce CO_2 to hydrocarbon products. However, the mechanisms of CO_2 reduction on nanostructured Cu catalysts are not well understood yet. In 2017, Tang et al. reported a copper-hydride nanocluster for CO_2RR to study the mechanism of Cu catalysts [72]. This $Cu_{32}H_{20}L_{12}$ NC (L = $S_2P(OiPr)_2$) comprises a distorted hexacapped rhombohedral core of 14 Cu atoms sandwiched by two Cu_9 triangular cupola fragments of Cu atoms, while the hydrides and L ligands are homogeneously distributed on the surface of the nanocluster (Fig. 2.18). The study on the CO_2 reduction mechanism shows that the key initial step of CO_2 reduction is where the first hydrogen is added: C or O of CO_2. The H addition on C would facilitate the formation of HCOOH, otherwise, CO would occur. Based on the structure of the Cu nanocluster, the authors proposed two possible channels to form the critical $HCOO^*$ intermediate: (1) the non-electrochemical absorption of CO_2 on lattice hydrides (lattice-hydride channel); (2) the electrochemical CO_2 reaction with proton and electron (proton-reduction channel). The free energy diagram of both channels for HCOOH and CO production shows that in both cases the lattice-hydride mechanism exhibits more energy downhill compared with the proton-reduction mechanism, suggesting the CO_2 reduction favors the lattice-hydride channel over this Cu NC. After the confirmation of reaction channel, the free energy diagram of CO and HCOOH formation is calculated following the lattice-hydride mechanism (Fig. 2.19a). The results indicate the HCOOH pathway is more favorable than the CO pathway over the Cu cluster.

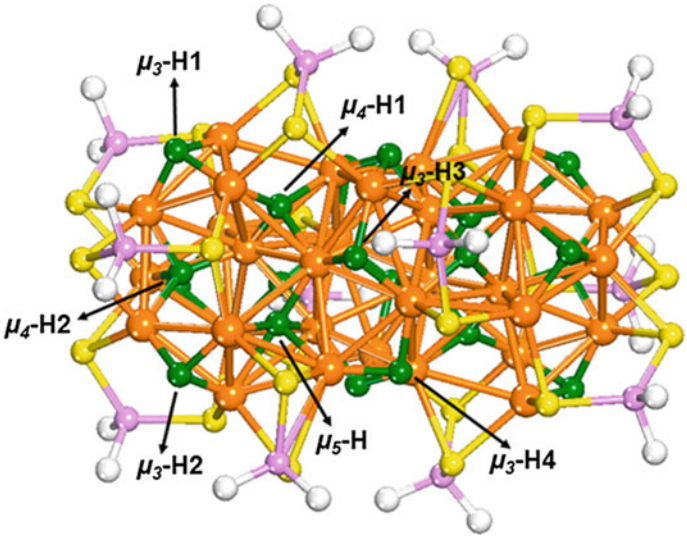

Fig. 2.18 Atomic structure of the $Cu_{32}H_{20}L_{12}$ NC (L = S_2PH_2). Orange, Cu; green, hydride; yellow, S; purple, P; white, H. Adapted with permission from Ref. [72]. Copyright 2017 American Chemical Society

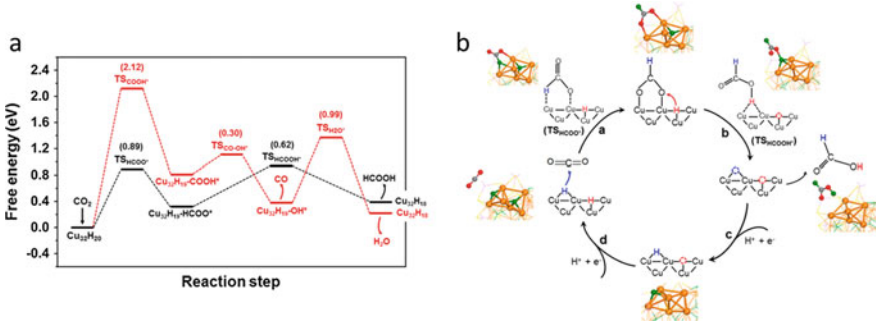

Fig. 2.19 **a** Free energy diagrams for HCOOH and CO formation on the $Cu_{32}H_{20}L_{12}$ NCs via the lattice-hydride mechanism, **b** overall mechanism of HCOOH formation from CO_2 reduction on $Cu_{32}H_{20}L_{12}$ NCs via the lattice-hydride channel, orange, Cu; green, hydride; red, oxygen; gray, carbon. Adapted with permission from Ref. [72]. Copyright 2017 American Chemical Society

Based on all the DFT calculation results, the authors proposed a complete catalytic mechanism as shown in Fig. 2.19d. It can be seen that the HCOOH is formed through the non-electrochemical lattice-hydride pathway. Additionally, the Cu NC can be recovered by the electrochemical reaction with two protons and electrons. Electrochemical tests are conducted to verify the theoretical prediction that HCOOH is favored over the Cu NC (Fig. 2.20). It can be seen that HCOOH is the dominant product at low potential with selectivity higher than 80%, while H_2 becomes dominant at high potential due to the competing HER. Only a small amount of CO is formed throughout the potential window. Therefore, these electrochemical results have successfully verified the accuracy of theoretical prediction. This work has demonstrated the methods of mechanism study using atomically precise metal

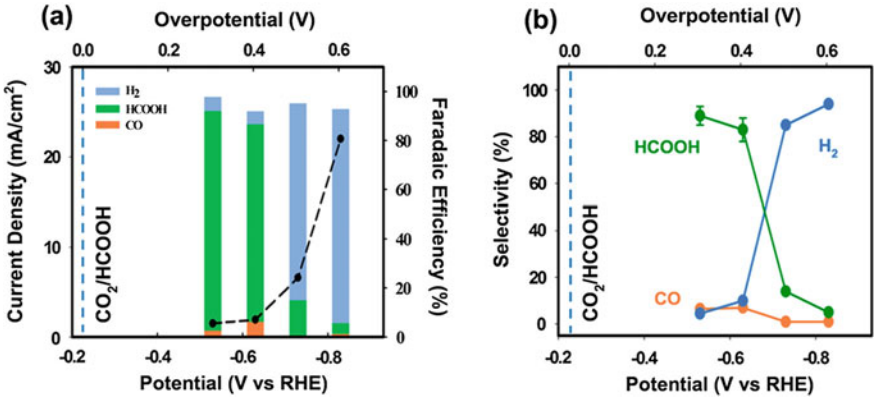

Fig. 2.20 **a** Average current densities (black) and cumulative FE for H_2, HCOOH and CO, **b** product selectivity for H_2, HCOOH and CO. Adapted with permission from Ref. [72]. Copyright 2017 American Chemical Society

NCs by combining DFT calculation and electrochemical experiment. Compared with traditional nanoparticles, the precise structure of nanoclusters makes the computational modeling much more facile and convincing. It is anticipated that the application of metal NCs in CO_2RR can offer insights in the mechanism study in the future.

2.7 Summary and Future Perspective

In this chapter, we have summarized the literature work about metal NCs as electrochemical catalysts. Compared with the metallic nanoparticles, the metal NCs exhibit discrete electronic energy levels due to the quantum size effect. This unique electronic property, plus atomically precise structures, as well as their various atom-packing structures, render the nanoclusters great potential in catalytic applications.

Metal nanoclusters (homogold and doped ones) have been demonstrated in several important electrochemical reactions including HER, OER, ORR, and CO_2RR. The results show that doping effects, synergetic effects, size effects, thermostability effects, charge effects, and morphology effects all play important roles in the catalytic effects. One of the most important advantages of nanoclusters in catalysis is the feasibility of computational modeling due to the available structure. For example, the catalytic mechanism of CO_2RR over $Cu_{32}H_{20}L_{12}$ NCs are predicted by DFT calculations and successfully verified by the electrochemical experiment. Metal nanoclusters are expected to be a promising class of model catalysts for correlating the structure and properties, providing exciting opportunities for the understanding of catalysis mechanism at the atomic level.

Future work in NCs electrocatalysis should investigate the following aspects:

(i) The doping effects. Several bimetallic NCs have been reported. However, the catalytic properties of bimetallic NCs are still rarely studied. The investigation of bimetallic NCs may be helpful to understand the impact of doping atoms, further revealing the fundamental catalytic mechanisms;

(ii) The synergetic effects. Au NCs-loaded composite materials are reported to show enhanced catalytic activity. It is essential to understand the interaction between supporting materials and metal NCs with more precise interfaces;

(iii) Metal NCs in other catalytic reactions. Owing to the characterized structure and tunable properties, metal NCs should be broadened to other catalytic reactions to study the fundamental catalytic mechanisms, such as nitrogen reduction reactions (NRR). The new electrocatalytic reactions remain to be explored.

References

1. Jin R, Zeng C, Zhou M, Chen Y (2016) Atomically precise colloidal metal nanoclusters and nanoparticles: fundamentals and opportunities. Chem Rev 116(18):10346–10413
2. Lu Y, Chen W (2012) Sub-nanometre sized metal clusters: from synthetic challenges to the unique property discoveries. Chem Soc Rev 41(9):3594–3623
3. Jin R (2010) Quantum sized, thiolate-protected gold nanoclusters. Nanoscale 2(3):343–362
4. Zeng C, Chen Y, Kirschbaum K, Lambright KJ, Jin R (2016) Emergence of hierarchical structural complexities in nanoparticles and their assembly. Science 354(6319):1580–1584
5. Qian H, Zhu M, Wu Z, Jin R (2012) Quantum sized gold nanoclusters with atomic precision. Acc Chem Res 45(9):1470–1479
6. Li G, Jin R (2013) Atomically precise gold nanoclusters as new model catalysts. Acc Chem Res 46(8):1749–1758
7. Turner JA (2004) Sustainable hydrogen production. Science 305(5686):972–974
8. Stambouli AB (2011) Fuel cells: The expectations for an environmental-friendly and sustainable source of energy. Renew Sustain Energy Rev 15(9):4507–4520
9. Das V, Padmanaban S, Venkitusamy K, Selvamuthukumaran R, Blaabjerg F, Siano P (2017) Recent advances and challenges of fuel cell based power system architectures and control–A review. Renew Sustain Energy Rev 73:10–18
10. Gasteiger HA, Kocha SS, Sompalli B, Wagner FT (2005) Activity benchmarks and requirements for Pt, Pt-alloy, and non-Pt oxygen reduction catalysts for PEMFCs. Appl Catal B 56(1–2):9–35
11. Costentin C, Robert M, Savéant J-M (2013) Catalysis of the electrochemical reduction of carbon dioxide. Chem Soc Rev 42(6):2423–2436
12. Qiao J, Liu Y, Hong F, Zhang J (2014) A review of catalysts for the electroreduction of carbon dioxide to produce low-carbon fuels. Chem Soc Rev 43(2):631–675
13. Vasileff A, Xu C, Jiao Y, Zheng Y, Qiao S-Z (2018) Surface and interface engineering in copper-based bimetallic materials for selective CO_2 electroreduction. Chem 4(8):1809–1831
14. Hori Y, Wakebe H, Tsukamoto T, Koga O (1994) Electrocatalytic process of CO selectivity in electrochemical reduction of CO_2 at metal electrodes in aqueous media. Electrochim Acta 39(11–12):1833–1839
15. Zhu W, Michalsky R, Metin ON, Lv H, Guo S, Wright CJ, Sun X, Peterson AA, Sun S (2013) Monodisperse Au nanoparticles for selective electrocatalytic reduction of CO_2 to CO. J Am Chem Soc 135(45):16833–16836
16. Lee H-E, Yang KD, Yoon SM, Ahn H-Y, Lee YY, Chang H, Jeong DH, Lee Y-S, Kim MY, Nam KT (2015) Concave rhombic dodecahedral Au nanocatalyst with multiple high-index facets for CO_2 reduction. ACS Nano 9(8):8384–8393
17. Zhu W, Zhang Y-J, Zhang H, Lv H, Li Q, Michalsky R, Peterson AA, Sun S (2014) Active and selective conversion of CO_2 to CO on ultrathin Au nanowires. J Am Chem Soc 136(46):16132–16135
18. Back S, Yeom MS, Jung Y (2015) Active sites of Au and Ag nanoparticle catalysts for CO_2 electroreduction to CO. Acs Catalysis 5(9):5089–5096
19. Zhao S, Jin R, Jin R (2018) Opportunities and challenges in CO_2 reduction by gold-and silver-based electrocatalysts: from bulk metals to nanoparticles and atomically precise nanoclusters. ACS Energy Lett 3(2):452–462
20. Zeng C, Chen Y, Kirschbaum K, Appavoo K, Sfeir MY, Jin R (2015) Structural patterns at all scales in a nonmetallic chiral Au_{133}(SR)52 nanoparticle. Sci Adv 1(2):e1500045
21. Higaki T, Zhou M, Lambright KJ, Kirschbaum K, Sfeir MY, Jin R (2018) Sharp transition from nonmetallic Au_{246} to metallic Au_{279} with nascent surface Plasmon resonance. J Am Chem Soc 140(17):5691–5695
22. Jin R, Qian H, Wu Z, Zhu Y, Zhu M, Mohanty A, Garg N (2010) Size focusing: a methodology for synthesizing atomically precise gold nanoclusters. J Phys Chem Lett 1(19):2903–2910
23. Zhu M, Aikens CM, Hollander FJ, Schatz GC, Jin R (2008) Correlating the crystal structure of a thiol-protected Au_{25} cluster and optical properties. J Am Chem Soc 130(18):5883–5885

24. Wu Z, Suhan J, Jin R (2009) One-pot synthesis of atomically monodisperse, thiol-functionalized Au 25 nanoclusters. J Mater Chem 19(5):622–626
25. Greeley J, Jaramillo TF, Bonde J, Chorkendorff I, Nørskov JK (2011) Computational high-throughput screening of electrocatalytic materials for hydrogen evolution. In: Materials for sustainable energy: a collection of peer-reviewed research and review articles from Nature Publishing Group. World Scientific, Singapore, pp 280–284
26. Kwak K, Choi W, Tang Q, Kim M, Lee Y, Jiang D-E, Lee D (2017) A molecule-like $PtAu_{24}(SC_6H_{13})$ 18 nanocluster as an electrocatalyst for hydrogen production. Nat Commun 8:14723
27. Choi W, Hu G, Kwak K, Kim M, Jiang D-E, Choi J-P, Lee D (2018) Effects of metal-doping on hydrogen evolution reaction catalyzed by MAu_{24} and M_2Au_{36} Nanoclusters (M=Pt, Pd). ACS Appl Mater Interfaces 10(51):44645–44653
28. Rountree ES, McCarthy BD, Eisenhart TT, Dempsey JL (2014) Evaluation of homogeneous electrocatalysts by cyclic voltammetry. ACS Publications
29. Valdez CN, Dempsey JL, Brunschwig BS, Winkler JR, Gray HB (2012) Catalytic hydrogen evolution from a covalently linked dicobaloxime. Proc Natl Acad Sci 109(39):15589–15593
30. Zhao S, Jin R, Song Y, Zhang H, House SD, Yang JC, Jin R (2017) Atomically precise gold nanoclusters accelerate hydrogen evolution over MoS_2 nanosheets: the dual interfacial effect. Small 13(43):1701519
31. Du Y, Xiang J, Ni K, Yun Y, Sun G, Yuan X, Sheng H, Zhu Y, Zhu M (2018) Design of atomically precise Au_2Pd_6 nanoclusters for boosting electrocatalytic hydrogen evolution on MoS_2. Inorganic Chem Front 5(11):2948–2954
32. Tahir M, Pan L, Idrees F, Zhang X, Wang L, Zou J-J, Wang ZL (2017) Electrocatalytic oxygen evolution reaction for energy conversion and storage: a comprehensive review. Nano Energy 37:136–157
33. Xia Z (2016) Hydrogen evolution: guiding principles. Nat Energy 1(10):16155
34. Gong M, Li Y, Wang H, Liang Y, Wu JZ, Zhou J, Wang J, Regier T, Wei F, Dai H (2013) An advanced Ni–Fe layered double hydroxide electrocatalyst for water oxidation. J Am Chem Soc 135(23):8452–8455
35. Zhuang Z, Sheng W, Yan Y (2014) Synthesis of monodispere $Au@Co_3O_4$ core-shell nanocrystals and their enhanced catalytic activity for oxygen evolution reaction. Adv Mater 26(23):3950–3955
36. Li Z, Ye K, Zhong Q, Zhang C, Shi S, Xu C (2014) Au–Co_3O_4/C as an efficient electrocatalyst for the oxygen evolution reaction. ChemPlusChem 79(11):1569–1572
37. Zhao S, Jin R, Abroshan H, Zeng C, Zhang H, House SD, Gottlieb E, Kim HJ, Yang JC, Jin R (2017) Gold nanoclusters promote electrocatalytic water oxidation at the nanocluster/$CoSe_2$ interface. J Am Chem Soc 139(3):1077–1080
38. Ramaswamy N, Mukerjee S (2011) Influence of inner-and outer-sphere electron transfer mechanisms during electrocatalysis of oxygen reduction in alkaline media. J Phys Chem C 115(36):18015–18026
39. Zhao S, Zhang H, House SD, Jin R, Yang JC, Jin R (2016) Ultrasmall palladium nanoclusters as effective catalyst for oxygen reduction reaction. ChemElectroChem 3(8):1225–1229
40. He Q, Cairns EJ (2015) Recent progress in electrocatalysts for oxygen reduction suitable for alkaline anion exchange membrane fuel cells. J Electrochem Soc 162(14):F1504–F1539
41. Guo S, Zhang S, Sun S (2013) Tuning nanoparticle catalysis for the oxygen reduction reaction. Angew Chem Int Ed 52(33):8526–8544
42. Cui C-H, Yu S-H (2013) Engineering interface and surface of noble metal nanoparticle nanotubes toward enhanced catalytic activity for fuel cell applications. Acc Chem Res 46(7):1427–1437
43. Li J, Yin H-M, Li X-B, Okunishi E, Shen Y-L, He J, Tang Z-K, Wang W-X, Yücelen E, Li C (2017) Surface evolution of a Pt–Pd–Au electrocatalyst for stable oxygen reduction. Nat Energy 2(8):17111
44. Sankarasubramanian S, Singh N, Mizuno F, Prakash J (2016) Ab initio investigation of the oxygen reduction reaction activity on noble metal (Pt, Au, Pd), Pt3M (M=Fe Co, Ni, Cu) and Pd3M (M=Fe Co, Ni, Cu) alloy surfaces, for LiO_2 cells. J Power Sources 319:202–209

45. Huang X, Zhao Z, Cao L, Chen Y, Zhu E, Lin Z, Li M, Yan A, Zettl A, Wang YM (2015) High-performance transition metal–doped Pt_3Ni octahedra for oxygen reduction reaction. Science 348(6240):1230–1234
46. Bu L, Zhang N, Guo S, Zhang X, Li J, Yao J, Wu T, Lu G, Ma J-Y, Su D (2016) Biaxially strained PtPb/Pt core/shell nanoplate boosts oxygen reduction catalysis. Science 354(6318):1410–1414
47. Zhang H, Jin M, Xiong Y, Lim B, Xia Y (2012) Shape-controlled synthesis of Pd nanocrystals and their catalytic applications. Acc Chem Res 46(8):1783–1794
48. Tang Z, Wu W, Wang K (2018) Oxygen reduction reaction catalyzed by noble metal clusters. Catalysts 8(2):65
49. Tang W, Lin H, Kleiman-Shwarsctein A, Stucky GD, McFarland EW (2008) Size-dependent activity of gold nanoparticles for oxygen electroreduction in alkaline electrolyte. J Phys Chem C 112(28):10515–10519
50. Zhang J, Sasaki K, Sutter E, Adzic R (2007) Stabilization of platinum oxygen-reduction electrocatalysts using gold clusters. Science 315(5809):220–222
51. Yin H, Tang H, Wang D, Gao Y, Tang Z (2012) Facile synthesis of surfactant-free Au cluster/graphene hybrids for high-performance oxygen reduction reaction. ACS Nano 6(9):8288–8297
52. Inasaki T, Kobayashi S (2009) Particle size effects of gold on the kinetics of the oxygen reduction at chemically prepared Au/C catalysts. Electrochim Acta 54(21):4893–4897
53. Lee Y, Loew A, Sun S (2009) Surface-and structure-dependent catalytic activity of Au nanoparticles for oxygen reduction reaction. Chem Mater 22(3):755–761
54. Wang L, Tang Z, Yan W, Yang H, Wang Q, Chen S (2016) Porous carbon-supported gold nanoparticles for oxygen reduction reaction: effects of nanoparticle size. ACS Appl Mater Interfaces 8(32):20635–20641
55. Chen W, Chen S (2009) Oxygen electroreduction catalyzed by gold nanoclusters: strong core size effects. Angew Chem Int Ed 48(24):4386–4389
56. Jones TC, Sumner L, Ramakrishna G, Hatshan M, Abuhagr A, Chakraborty S, Dass A (2018) Bulky t-Butyl thiolated gold nanomolecular series: synthesis, characterization, optical properties, and electrocatalysis. J Phys Chem C 122(31):17726–17737
57. Negishi Y, Chaki NK, Shichibu Y, Whetten RL, Tsukuda T (2007) Origin of magic stability of thiolated gold clusters: a case study on $Au_{25}(SC_6H_{13})_{18}$. J Am Chem Soc 129(37):11322–11323
58. Zhu M, Eckenhoff WT, Pintauer T, Jin R (2008) Conversion of anionic $[Au_{25}(SCH_2CH_2Ph)_{18}]^-$ cluster to charge neutral cluster via air oxidation. J Phys Chem C 112(37):14221–14224
59. Zhu M, Aikens CM, Hendrich MP, Gupta R, Qian H, Schatz GC, Jin R (2009) Reversible switching of magnetism in thiolate-protected Au_{25} superatoms. J Am Chem Soc 131(7):2490–2492
60. Qian H, Sfeir MY, Jin R (2010) Ultrafast relaxation dynamics of $[Au_{25}(SR)_{18}]^q$ nanoclusters: effects of charge state. J Phys Chem C 114(47):19935–19940
61. Lu Y, Jiang Y, Gao X, Chen W (2014) Charge state-dependent catalytic activity of $[Au_{25}(SC_{12}H_{25})_{18}]$ nanoclusters for the two-electron reduction of dioxygen to hydrogen peroxide. Chem Commun 50(62):8464–8467
62. Mills G, Gordon MS, Metiu H (2003) Oxygen adsorption on Au clusters and a rough Au (111) surface: the role of surface flatness, electron confinement, excess electrons, and band gap. 118(9):4198–4205
63. Vickers JW, Alfonso D, Kauffman DR (2017) Electrochemical carbon dioxide reduction at nanostructured gold, copper, and alloy materials. Energy Technol 5(6):775–795
64. Kim D, Resasco J, Yu Y, Asiri AM, Yang P (2014) Synergistic geometric and electronic effects for electrochemical reduction of carbon dioxide using gold–copper bimetallic nanoparticles. Nat Commun 5:4948
65. Geng Z, Kong X, Chen W, Su H, Liu Y, Cai F, Wang G, Zeng J (2018) Oxygen vacancies in ZnO nanosheets enhance CO_2 electrochemical reduction to CO. Angew Chem Int Ed 57(21):6054–6059

66. Zhang L, Zhao ZJ, Gong J (2017) Nanostructured materials for heterogeneous electrocatalytic CO_2 reduction and their related reaction mechanisms. Angew Chem Int Ed 56(38):11326–11353
67. Xie H, Wang T, Liang J, Li Q, Sun S (2018) Cu-based nanocatalysts for electrochemical reduction of CO_2. Nano Today 21:41–54
68. Kauffman DR, Alfonso D, Matranga C, Qian H, Jin R (2012) Experimental and computational investigation of Au_{25} clusters and CO_2: a unique interaction and enhanced electrocatalytic activity. J Am Chem Soc 134(24):10237–10243
69. Alfonso DR, Kauffman D, Matranga C (2016) Active sites of ligand-protected Au_{25} nanoparticle catalysts for CO_2 electroreduction to CO. J Chem Phys 144(18):184705
70. Kauffman DR, Thakkar J, Siva R, Matranga C, Ohodnicki PR, Zeng C, Jin R (2015) Efficient electrochemical CO_2 conversion powered by renewable energy. ACS Appl Mater Interfaces 7(28):15626–15632
71. Zhao S, Austin N, Li M, Song Y, House SD, Bernhard S, Yang JC, Mpourmpakis G, Jin R (2018) Influence of atomic-level morphology on catalysis: The case of sphere and rod-like gold nanoclusters for CO_2 electroreduction. ACS Catalysis 8(6):4996–5001
72. Tang Q, Lee Y, Li D-Y, Choi W, Liu C, Lee D, Jiang D-E (2017) Lattice-hydride mechanism in electrocatalytic CO_2 reduction by structurally precise copper-hydride nanoclusters. J Am Chem Soc 139(28):9728–9736